

EFFECT OF THE IRON OXIDE CONTENT ON THE STRUCTURE AND ALKALI RESISTANCE OF GLASS FIBRES PREPARED FROM RED MUD

CHEN ZISHENG*, **, SUN CHUANXIANG*, **, XU ZHAOZHI*, **, WANG LONGJUN*, **, QU YA*, ZHANG WEIJUAN*, #YUE YUNLONG*, **, #KANG JUNFENG*

*School of Materials Science and Engineering, University of Jinan, Jinan, 250000, China

**Shandong Institutes of Industrial Technology, Jinan, 250000, China

#E-mail: zztg_yueyl@163.com, mse_kangjf@ujn.edu.cn

Submitted March 6, 2023; accepted April 7, 2023

Keywords: Tensile strength, Alkali resistance, Red mud, Glass fibre

In this work, glass fibres with red mud, as the main raw material, were prepared. The effect of the iron oxide content on the structure and alkali resistance of the glass fibres was studied by XPS, FT-IR, DSC, SEM-EDS, while the tensile strength and mass loss rate in alkali corrosion were also analysed. The results showed iron existed mainly in the form of Fe^{3+} . The network polymerisation degree of the glasses decreased as the SiO_2/Fe_2O_3 mass ratio (Si/Fe) decreased, which caused a significant reduction in the T_g and the thermal stability parameter ΔT ($\Delta T = T_c - T_g$). The fibre tensile strength deteriorated when the Si/Fe ratio decreased, while the alkali resistance of the fibres strengthened. After 72 h of alkali corrosion, the average tensile strength of fibres decreased significantly, which were all below 500 MPa. The SEM combined with EDS analysis revealed the shell formed on the fibre surface was mainly oxides and hydroxides of insoluble metals (Fe, Ca), preventing further corrosion by OH⁻.

INTRODUCTION

Red mud, a kind of solid waste, is produced by factories in the process of producing alumina [1]. When 1 t of alumina is produced, 1 – 2 t of red mud will be made [2]. Due to red mud having a strong alkaline effect [3, 4] and its large output and low utilisation rate, the most common treatment method at present is red mud disposal [5], which causes serious pollution to the surrounding soil and groundwater [6-8]. Therefore, it is a global issue to find a way to fully utilise and effectively recover red mud. Recently, many scholars have conducted a great deal of experiments and studies on the utilisation of red mud. Mandal et al. [9] prepared insulating bricks by mixing red mud and wood chips, and the best performance was achieved when the wood chip content was 7.5 %. Jiling. Zhao et al. [10] improved the durability of red mud glass by adding SnO_2 and the best performance was achieved when the SnO_2 was 1.48 wt. %. Huizhi. Yang et al. [11] prepared glass ceramics by mixing 20 % – 50 % of red mud, which had better mechanical, acid and alkali corrosion resistance properties. KRITIKAKI et al. [12] prepared glass ceramics using red mud, fly ash and slag, and compared the properties of the products with different doping levels, which provided a reference for industrial use of solid waste for the preparation of glass ceramics.

Red mud is mainly composed of SiO_2 , Fe_2O_3 , Al_2O_3 , CaO and Na_2O , which is similar to the composition of basalt. Therefore, in this work, similar to basalt, fibres are prepared by adjusting the components, which are then applied in fibre-reinforced concrete. Mixing the fibres into the concrete makes the concrete tougher and more impact resistant [13, 14], but concrete mortars are usually highly alkaline ($pH \geq 12.5$), which means that the fibres need to have high alkali resistance. Therefore, the glass fibres prepared in this experiment use red mud as the raw material. Then, by changing the iron oxide content of the glass fibres, the changes in the mechanical properties and alkali resistance are measured. Moreover, the effects of the changes of the iron oxide content on the structure and alkali resistance of the glass fibres are analysed.

EXPERIMENTAL

Preparation

Glass samples were produced by a high-temperature melting method, and the raw materials were red mud, quartz powder, dolomite and industrial alumina. The components of each raw material were tested by an X-ray fluorescence spectrometer (XRF, Bruker S8 TIGER), and the composition is shown in Table 1.

Table 1. Composition of the raw materials (wt. %).

	SiO ₂	Al ₂ O ₃	Fe ₂ O ₃	CaO	Na ₂ O	TiO ₂	MgO	LOI
Red mud	20.58	25.48	11.70	13.97	6.55	4.14	0.22	17.36
Quartz powder	98.80	0.74	0.13	—	0.03	—	—	0.30
Dolomite	0.50	0.15	0.05	31.40	—	—	20.80	47.10
Industrial alumina	—	99.07	0.01	—	0.42	—	—	0.50

Table 2. Composition of the glass samples of the SF group (wt. %).

No.	SiO ₂	Al ₂ O ₃	Fe ₂ O ₃	CaO	Na ₂ O	TiO ₂	MgO	SiO ₂ /Fe ₂ O ₃
SF-1	59.03	15.52	3.51	10.09	5.57	1.24	3.82	16.82
SF-2	58.06	15.59	4.10	10.09	5.59	1.45	3.82	14.16
SF-3	57.09	15.57	4.68	10.09	5.52	1.66	3.83	12.20
SF-4	56.02	15.55	5.27	10.09	5.55	1.86	3.83	10.63
SF-5	55.05	15.52	5.85	10.09	5.58	2.07	3.83	9.41

Glass samples preparation

Table 2 shows the composition of the glass samples, which is labelled as SF-1 to SF-5 according to the mass ratio of SiO₂ to Fe₂O₃ (referred to as Si/Fe). The glass batches were placed into the alumina crucible according to the calculated components, and then heated at 1500 – 1550 °C for 3 h. The molten glass was poured onto a graphite plate into a mould and removed to a muffle furnace, which annealed it for 2 h at the glass transition temperature. Then, the base glasses were obtained by cooling to room temperature.

Glass fibre preparation

About 50 g of the glass was placed in a corundum crucible with a hole in the bottom (the hole is 6 mm in diameter). Glass fibres were drawn at the fibre-forming temperature using fibre drawing equipment and then collected on a rotating wheel with a constant speed. The spinning speed range was 125.6 – 376.9 m·min⁻¹. Glass fibres with a diameter of 35 ± 5 µm were selected for the subsequent test experiments.

Characterisation

An X-ray diffraction (XRD) analyser (D8 ADVANCE) was used to determine that the glass samples are amorphous, using Cu-K_α rays in the range of 10 – 80° at 2°·min⁻¹.

An X-ray photoelectron spectrometer (XPS, ESCALAB Xi+, UK) from Thermo Fisher Scientific was used to analyse the valence states of the atoms in the samples, with Al K_α as the excitation source, which was measured at a constant target voltage and target current (15 kV, 10 mA) [15].

The structure of the sample was analysed using an infrared spectrometer (Nicolet-380), in which the KBr press method was used. The wavelength range of the test was 400 – 1600 cm⁻¹.

The density of the samples was tested at room temperature using a densitometer (AR233CN), based on Archimedes' principle [16]. The tests were repeated at least three times for each group of samples to reduce the error.

The thermal properties of the samples were analysed using differential scanning calorimetry (DSC, Netzsch STA 409, Germany). The temperature range was 20 – 1200 °C, and the heating rate was controlled at 10 °C·min⁻¹.

The glass fibre tensile strength reflects the ability of the material to resist fracture. The calculation formula is shown in Equation (1). The fibre diameter was measured using an optical microscope and the fibre tensile strength at breakage was measured using a fibre tensiometer (GFLS-98).

$$\sigma = \frac{F}{S} \quad (1)$$

where, σ is the fibre tensile strength, MPa. F is the tensile force of the fibre at breakage. S is the cross-sectional area of the fibre.

Glass fibres with a length of about 6 cm and a weight of about 2 g were intercepted in each group for the alkali resistance test. The fibres were placed in centrifuge tubes containing a 1 mol·L⁻¹ NaOH solution (pH = 14), and heated in a water bath at 80 °C for 12 h, 24 h, 48 h and 72 h, respectively. The samples were cleaned with flowing water and then dried in a drying oven at 80 °C. After drying, the mass loss of the samples was measured. The mass loss rate is calculated by Equation 2 as shown below. Scanning electron microscopy (SEM, QUANTA 250) was used observe the morphology

of the fibres after corrosion, and energy dispersive spectroscopy (EDS) was used to analyse the compositional changes of the fibres.

$$M = \frac{M_1 - M_2}{M_1} \times 100\% \quad (2)$$

where M is the mass loss rate, M_1 is the mass of the uncorroded sample and M_2 is the mass of the corroded sample.

RESULTS AND DISCUSSION

XRD

The XRD patterns of the samples are shown in Figure 1. There is no sharp diffraction peak in the figure, indicating that all the samples are in the amorphous state.

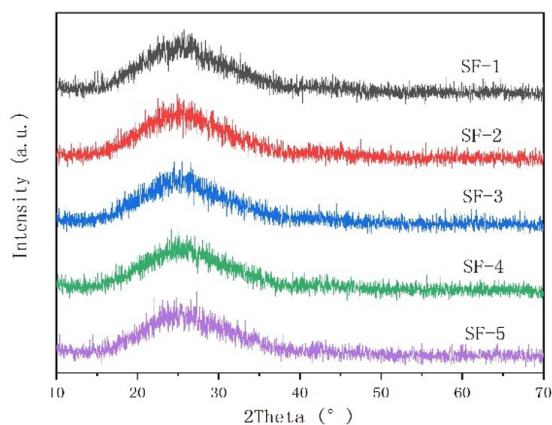


Figure 1. XRD pattern of the SF group samples.

XPS analysis

Figure 2 shows the XPS spectra of the glass samples. As shown in the figures, the binding energy of Fe^{3+} is around 711.5 eV, usually accompanied by the presence of satellite peaks, and that of Fe^{2+} is around 724.6 eV [15, 17, 18], which is consistent with the results of Toru Yamashita et al. [19] and, after calculation, the proportion of Fe^{3+} to the total number of ferrous ions in the three groups of samples is almost unchanged ($\text{Fe}^{3+}:\text{Fe}_{\text{total}} = 0.7$). Therefore, the experiments mainly discussed the effect of Fe^{3+} on the glass fibres, including the mechanical properties and alkali resistance.

FTIR spectra

Figure 3 shows the IR spectra of the glass samples. In the range of 400 - 1600 cm^{-1} , the samples exhibit three main characteristic absorption bands at about 460, 710 and 1020 cm^{-1} . About 460 cm^{-1} , the first absorption band can be seen, which is due to the bending vibrations of Si-O-Si and Al-O-Si [20]. The 600 - 850 cm^{-1}

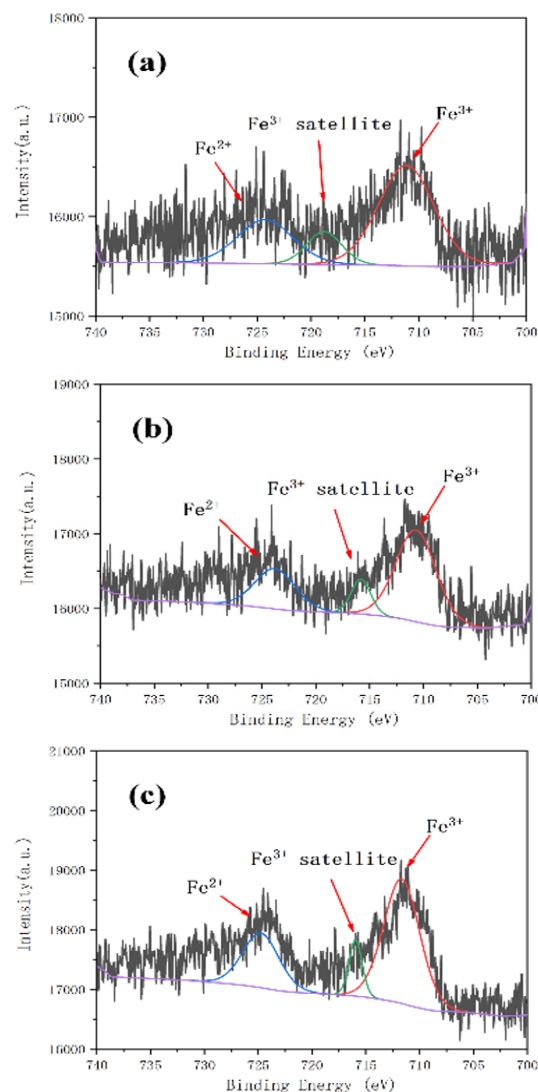


Figure 2. (a) XPS spectra of SF-1, (b) XPS spectra of SF-3, (c) XPS spectra of SF-5.

absorption band represents the stretching vibration of T-O-T (T = Si, Al, Fe) in the tetrahedral network [21]. The 850 - 1300 cm^{-1} absorption band results from the antisymmetric stretching vibrations of the Si-O-Si and Si-O bonds [22, 23]. When the iron oxide content increases, the absorption band around 1020 cm^{-1} is transferred to a lower wavenumber. This is due to the reduction in the number of Si-O-Si bonds, resulting in a decrease in the connectivity of the glass network. Meanwhile, the absorption band around 710 cm^{-1} is flattened, which indicates a decrease in the number of tetrahedral structures [20]. In general, first of all, the reduction in the SiO_2 content results in a decrease in the connectivity of the glass network. Secondly, the free oxygen provided by the iron oxide increases the amount of non-bridging oxygen (NBO), causing a reduction in the connectivity of the $[\text{SiO}_4]$ tetrahedra [24], and the network structure is further damaged.

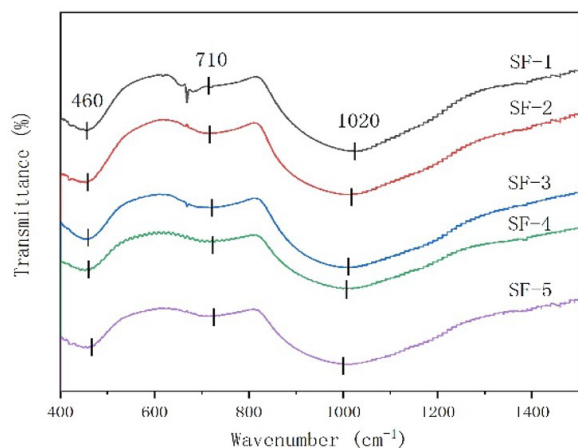


Figure 3. FTIR spectra of glass samples from the SF group.

Density

Density is an important property of glass. The density of the glass samples is shown in Figure 4. With an increase in the iron oxide content in the samples, the density of the samples shows an increasing trend, from $2.602 \text{ g}\cdot\text{cm}^{-3}$ to $2.675 \text{ g}\cdot\text{cm}^{-3}$.

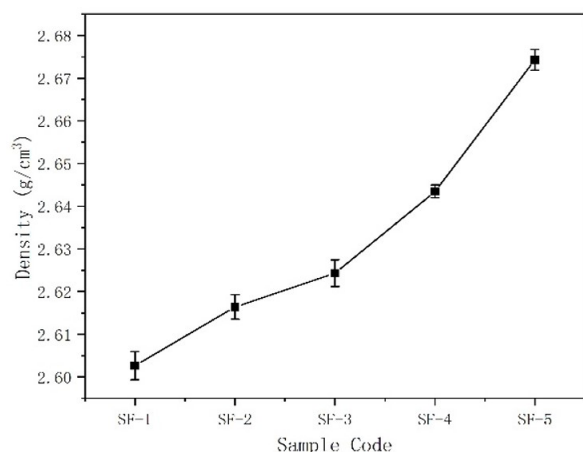


Figure 4. Density of the glass samples of the SF group.

DSC

Figure 5 shows the DSC curves for SF-1 to SF-5. The characteristic temperatures of the glass (glass transition temperature T_g , the crystallisation onset temperature T_c , the crystallisation peak temperature T_p and liquid temperature T_l) are measured by DSC. The values are shown in Table 3, where $\Delta T = T_c - T_g$. It can be seen from Figure 5 and Table 3 that T_g gradually decreases with the increasing iron oxide, from $726 \text{ }^\circ\text{C}$ to $705 \text{ }^\circ\text{C}$. The glass transition temperature usually reflects the tightness of the glass network, and is related to the amount of bridging oxygen (BO) in the $[\text{SiO}_4]$ and $[\text{AlO}_4]$ tetrahedra. According to the structural analysis, the increase in the iron

oxide makes the NBOs in the glass structure increase and the glass structure becomes loose, resulting in a significant decrease in T_g . ΔT is a parameter that measures the resistance to crystallisation [25]. From Table 3, it can be seen that ΔT decreases with a decreasing Si/Fe ratio, which indicates that the glass becomes worse in terms of its thermal stability, and the glass becomes easier to crystallise.

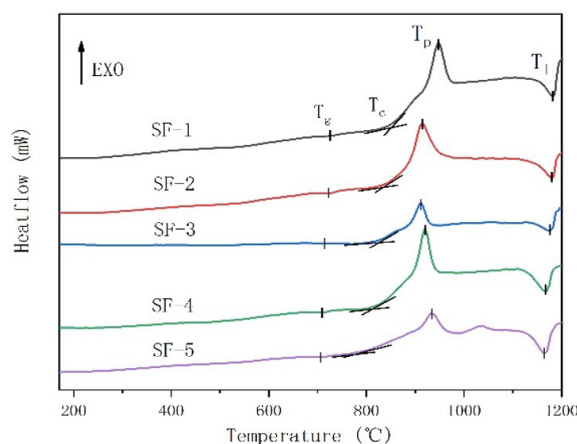


Figure 5. The DSC curves of the SF group samples.

 Table 3. The characteristic temperatures ($^\circ\text{C}$) of the glass samples of the SF group from the DSC curve.

No.	T_g	T_c	T_p	T_l	ΔT
SF-1	726	849	948	1183	123
SF-2	722	833	915	1179	111
SF-3	714	826	912	1174	112
SF-4	710	814	919	1165	104
SF-5	705	778	922	1162	73

Tensile strength testing of the raw glass fibres

In order to evaluate the glass fibre tensile strength, a Weibull distribution model was used for the analysis. It is based on the “weakest link theory” and assumes that independent defects at random locations cause mechanical failures [26]. The cumulative failure probability distribution function (P) is defined as

$$P = 1 - \exp \left[- \left(\frac{\sigma}{\eta} \right)^\beta \right] \quad (3)$$

where σ is the independent variable, which can be expressed as the fibre tensile strength for the glass fibres. β is the shape parameter, indicating the dispersion of the fibre tensile strength, when the value of β is large, the failure stress range of fibres is narrower. η is the scale parameter, its value represents the growth rate of the failure probability, when the value of η is larger, the growth rate is slower. P is the failure probability.

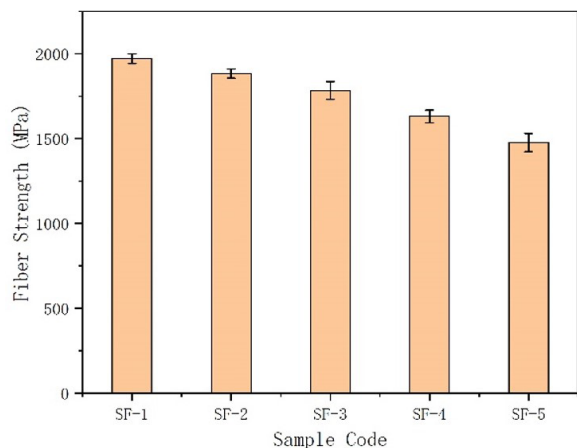


Figure 6. Tensile strength of the glass fibres in the SF group.

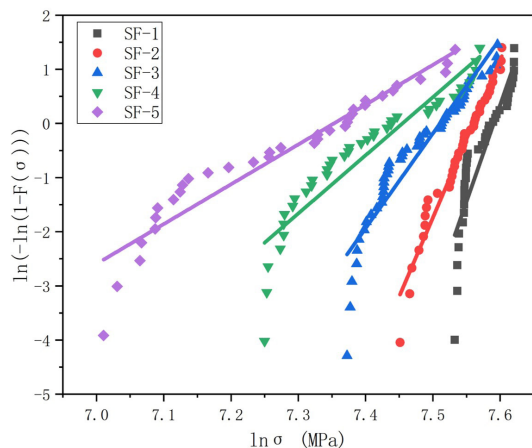


Figure 7. Weibull function distribution of the tensile strength of the glass fibres in the SF group.

Table 4. Fitting parameters of the Weibull distribution function for the SF group.

Parameters	β	η
SF-1	35.66	1979.07
SF-2	29.09	1919.50
SF-3	17.52	1827.14
SF-4	10.74	1728.26
SF-5	7.35	1560.62

At least 30 samples of each group of glass fibres were selected for measurement and the results are shown in Figure 6. The fibre tensile strength gradually decreased with the increasing iron oxide content, from 1949 ± 28 MPa to 1464 ± 53 MPa, which has the same trend as the study by Gutnikov et al. [27]. Figure 7 shows the Weibull distribution function of the fibres and its fitted parameters are summarised in Table 4. Combined with Figure 7 and Table 4, with the increase in the iron oxide content, the β and η values gradually decrease. It indicates that the range of failure stress of the fibres becomes wider [28] and the growth rate of failure probability becomes faster. In other

words, the distribution range of the fibre diameter becomes larger and the stability of the fibre strength becomes worse.

Alkali resistance test of the glass fibre

In alkaline solutions, the OH^- in the solution reacts with SiO_2 and Al_2O_3 to form dissoluble salts. The reaction equations are as follows [29-32].

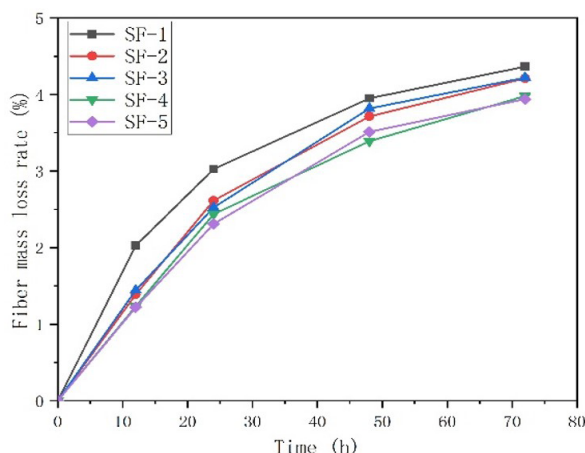
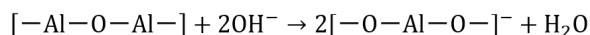


Figure 8. Mass loss rate of the glass fibre in the NaOH solution for the SF group.

Figure 8 shows the mass loss rate of the glass fibre samples after corrosion. The mass loss of the glass fibres increases with an increase in the corrosion time, but the mass loss rate tends to be flat. Moreover, the mass loss rate with the same corrosion time is roughly in the following order: SF-1 > SF-2 > SF-3 > SF-4 > SF-5. The highest mass loss rate of 4.36 % was observed for SF-1 after 72 h of corrosion.

Figure 9 shows the optical microscope diagram of the SF-1 group of glass fibres with different corrosion times. At 12 h of corrosion, the surface of the fibres only appeared as “sesame seed” spots. The spots increased in number and became bigger after 24 h of corrosion. After 48 h of corrosion, the corrosion further deepened, the fibre surface also gradually formed a brittle shell. At the corrosion time of 72 h, the brittle shell on the fibre surface appears to partially peeled off. It is also the reason for the loss of mass of the fibre after corrosion by the alkali solution.

Figure 10a shows the SEM image of the glass fibres of the SF-1 group after corrosion for 72 h. Figure 10b and c show the EDS analysis of the corroded glass fibres at points A and B. Table 5 shows the results of the EDS analysis. From the SEM diagram, it can be seen that a shell of constant thickness is formed on the glass fibre surface, which appeared to be peeling in some areas.

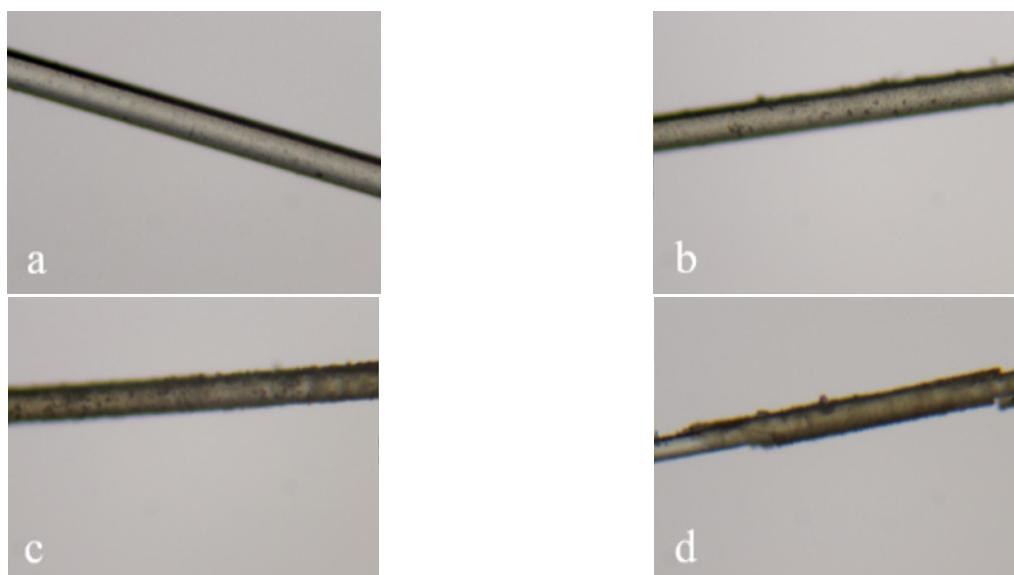


Figure 9. Optical micrographs of the different corrosion times of the SF-1 group fibres: (a) 12 h, (b) 24 h, (c) 48 h, (d) 72 h.

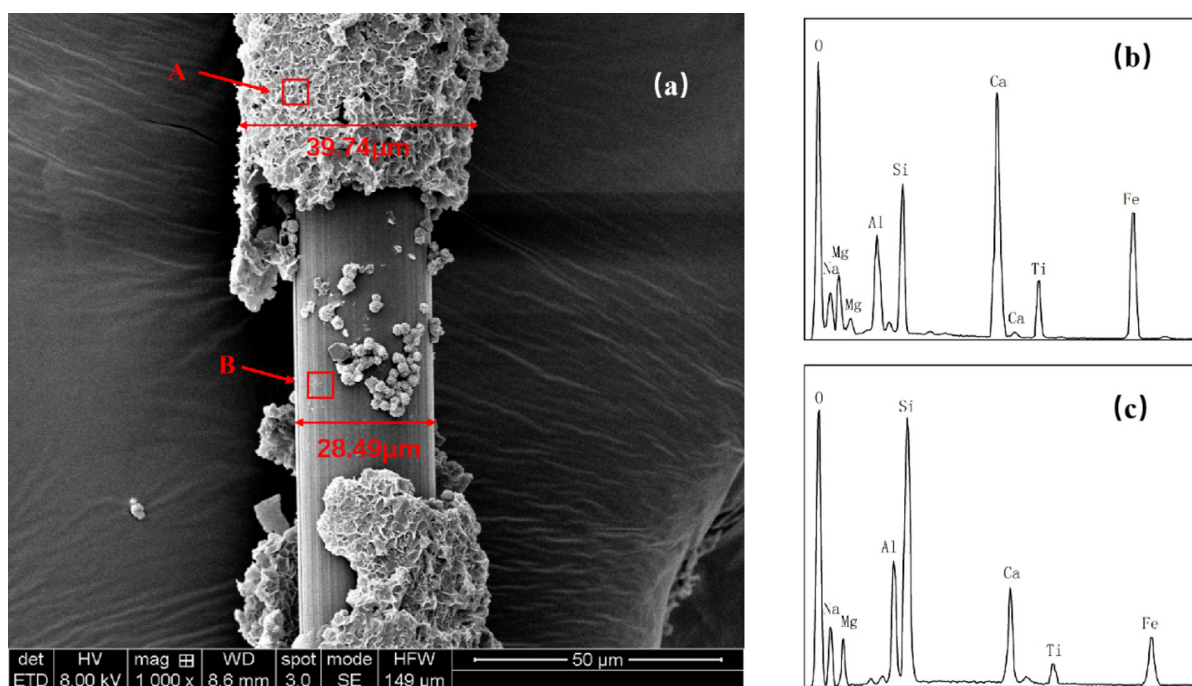


Figure 10. (a) SEM diagram of the SF-1 group glass fibre corrosion for 72 h, (b) EDS analysis of point A, (c) EDS analysis of point B.

The fibre diameter is also reduced from 39.74 μm to 28.49 μm after measurement. Combined with the EDS analysis results, it can be determined that the shell is generated by the reaction of the glass fibre with the alkali solution.

Comparing the oxide content of the glass fibres at different locations in Table 5, the composition is found to be significantly different. Compared with the fresh fibre, SiO_2 , Al_2O_3 , and Na_2O of the glass fibre at point A are significantly reduced, while the iron oxide and CaO contents are significantly increased, and the MgO and TiO_2 contents are also slightly increased. The reason for this phenomenon is that

the OH^- in alkaline solutions reacts with the silica-oxygen tetrahedra to form silicate ions that release into the solution [33], which is the main reason for the high fibre mass loss. While the silicon-oxygen tetrahedra are destroyed, the number of NBOs increases. Then, the corrosion proceeds further and the Al-O structure is also destroyed into the solution [34, 35], which results in a decrease in the Al_2O_3 content in the corrosion shell. The Na^+ that existed in the gaps of the glass network will be dissolved out as the glass network structure will be destroyed. Fe^{3+} as a network intermediate will play the role of a complementary network to form Fe-O, which will form a more stable fibre skeleton structure

Table 5. Comparison of the fibre EDS analysis results with the fresh fibre composition (wt. %).

	Fresh fibre	A	B
SiO ₂	59.03	27.38	58.28
Al ₂ O ₃	15.52	6.34	16.72
Fe ₂ O ₃	3.51	15.72	4.16
Na ₂ O	5.57	1.19	4.87
CaO	10.09	41.31	11.50
MgO	3.82	4.52	3.53
TiO ₂	1.24	3.06	0.92

[36], the position in the fibre is more solid, but not easy to dissolve, so the iron oxide content in the corrosion shell is much higher than the original filament content.

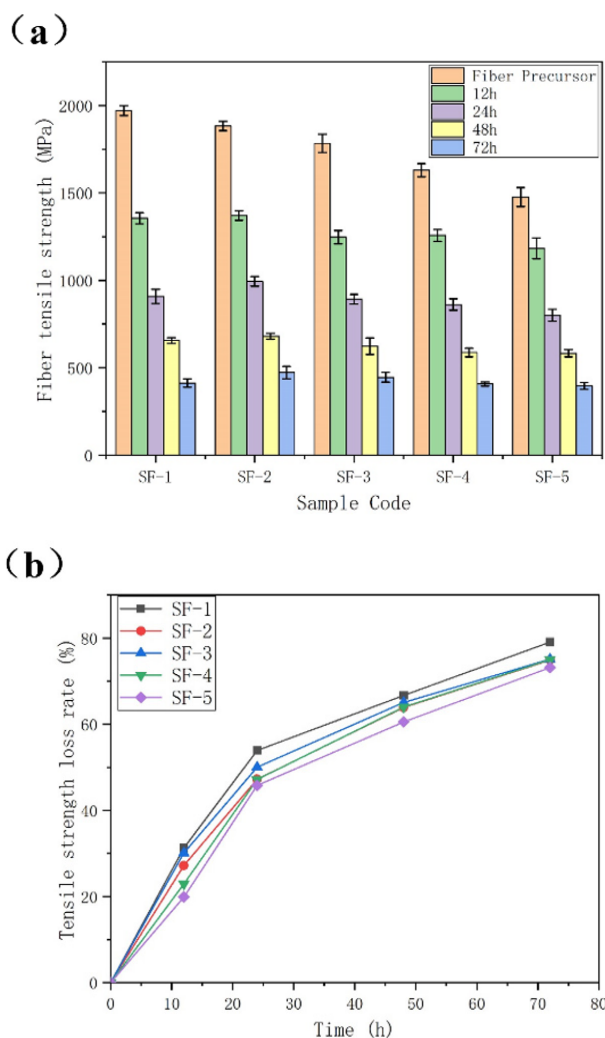


Figure 11. (a) Fibre tensile strength before and after alkali corrosion for the SF group, (b) Fibre strength loss rate for the SF group.

Figure 11a shows the comparison of the fibre tensile strength before and after the alkali corrosion, and b shows the rate of the fibre strength loss. As shown in Figure 11a, the fibre tensile strength of each group

after corrosion with the alkali solution is substantially reduced, and the average tensile strength of each group of fibres was below 500 MPa after 72 h of corrosion. The fibres of the SF-1 group have the largest strength loss rate of 79.1 % after 72 h of corrosion, and the smallest loss rate of 73.2 % is in SF-5 group, which can be clearly seen in Figure 11b. The loss of tensile strength of the fibres in the SF group is negatively correlated with the iron oxide content. This is due to the increase in the iron oxide content and the increase in the formation of spherical Fe³⁺ and Ca²⁺ particles on the fibre surface. These particles are insoluble metal (Fe, Ca) oxides and hydroxides, which subsequently enrich into large lamellar shells on the fibre surface [37], preventing any further corrosion by OH⁻. The increase in the iron oxide will improve the alkali resistance of the glass, but more Fe ions will lead to the spontaneous crystallisation of the glass melt during the fibre formation, which will increase the number of defects on the fibre surface and the fibre tensile strength will be reduced [38].

CONCLUSIONS

In this work, the effect of increasing the iron oxide content on the structure and properties of red mud glass fibres was discussed. The FT-IR results showed that the connection degree of the glass network decreased and the glass structure was destroyed as the mass ratio of SiO₂/Fe₂O₃ (Si/Fe) decreased. According to the DSC results, the increase in the iron oxide content made the thermal stability parameter ΔT smaller and the thermal stability worse, so that the glass was more prone to crystallisation. We tested the alkali resistance and mechanical properties of the glass fibres, and the results showed that the fresh fibre tensile strength gradually decreased as the Si/Fe ratio decreased, but the alkali resistance of the fibres increased. On one hand, the SiO₂ reduction leads to the glass network structure being destroyed. Meanwhile, the increase in the iron oxide content makes the NBOs increase and the network structure is further disrupted. The tensile strength eventually shows a decreasing trend. On the other hand, Fe³⁺ and Ca²⁺ form insoluble oxides and hydroxides on the fibre surface, which, in turn, form large lamellar shells and prevent any further corrosion of the fibre by OH⁻. However, after a long period of alkali corrosion, the average fibre tensile strength decreased significantly, and the final strengths were all below 500 MPa, with the highest strength loss rate of 79.1 % and the lowest of 73.2 % for SF-5. Therefore, in the actual production process, both parts should be considered.

Acknowledgments

This paper was funded by National Natural Science Foundation of China (No. 52072148) (No. 52172019) (No. 51804131) and the Opening Project of State Key Laboratory of Advanced Technology for Float Glass (No. 2020KF01).

REFERENCES

- Gupta V. K., Gupta M., Sharma, S. (2001): Process development for the removal of lead and chromium from aqueous solutions using red mud—an aluminium industry waste. *Water Research*, 35(5), 1125-1134. Doi: 10.1016/S0043-1354(00)00389-4
- Wang L., Sun N., Tang H., Sun W. (2019): A review on comprehensive utilization of red mud and prospect analysis. *Minerals*, 9(6), 362. Doi: 10.3390/min9060362
- Li L.Y. (2001): A study of iron mineral transformation to reduce red mud tailings. *Waste management*, 21(6), 525-534. Doi: 10.1016/S0956-053X(00)00107-0
- Tsakiridis P. E., Agatzini-Leonardou S., Oustadakis, P. (2004): Red mud addition in the raw meal for the production of Portland cement clinker. *Journal of Hazardous Materials*, 116(1-2), 103-110. Doi: 10.1016/j.jhazmat.2004.08.002
- Zhang T. A., Wang Y., Lu G., Liu Y., Zhang W., Zhao Q. (2018): Comprehensive utilization of red mud: current research status and a possible way forward for non-hazardous treatment. *Light metals 2018*, 135-141. Doi: 10.1007/978-3-319-72284-9_18
- Wei F. N., Guo L. Y., Liu Z. C., Shen X., Liu H. T. (2012): Thermogravimetric analysis of desulfurization characteristics and kinetic parameters of limestone modified by red mud. In *Advanced Materials Research* (Vol. 512, pp. 2339-2342). Trans Tech Publications Ltd. Doi:10.4028/www.scientific.net/amr.512-515.2339
- Brunori C., Cremisini C., Massanisso P., Pinto V., Torricelli L. (2005): Reuse of a treated red mud bauxite waste: studies on environmental compatibility. *Journal of Hazardous materials*, 117(1), 55-63. Doi: 10.1016/j.jhazmat.2004.09.010
- Liang G., Chen W., Nguyen A. V., Nguyen T. A. (2018): Red mud carbonation using carbon dioxide: Effects of carbonate and calcium ions on goethite surface properties and settling. *Journal of Colloid and Interface Science*, 517, 230-238. Doi: 10.1021/acs.langmuir.7b03589
- Mandal A. K., Verma H. R., Sinha O. P. (2017): Utilization of aluminum plant's waste for production of insulation bricks. *Journal of Cleaner Production*, 162, 949-957. Doi: 10.1016/j.jclepro.2017.06.080
- Zhao J., Wang Y., Kang J., Qu Y., Khater G. A., Li S., et al. (2019): Effect of SnO₂ on the structure and chemical durability of the glass prepared by red mud. *Journal of Non-Crystalline Solids*, 509, 54-59. Doi:10.1016/j.jnoncrsol.2019.01.029
- Yang H.Z., et al. (2007). *Preparation of the red mud glass-ceramics by sintering process*. Light Metals.
- Kritikaki A., Zaharaki D., Komnitsas K. (2016): Valorization of industrial wastes for the production of glass-ceramics. *Waste and Biomass Valorization*, 7, 885-898. Doi:10.1007/s12649-016-9480-x
- Mohammadi Y., Singh S. P., Kaushik S. K. (2008): Properties of steel fibrous concrete containing mixed fibres in fresh and hardened state. *Construction and Building Materials*, 22(5), 956-965. Doi: 10.1016/j.conbuildmat.2006.12.004
- Yazıcı Ş., İnan G., Tabak V. (2007): Effect of aspect ratio and volume fraction of steel fiber on the mechanical properties of SFRC. *Construction and Building Materials*, 21(6), 1250-1253. Doi:10.1016/j.conbuildmat.2006.05.025
- Jensen M., Zhang L., Yue Y. (2012): Probing iron redox state in multicomponent glasses by XPS. *Chemical Geology*, 322, 145-150. Doi: 10.1016/j.chemgeo.2012.07.007
- Zamyatin O. A., Plekhovich A. D., Zamyatina E. V., Sibirkin A. A. (2016): Glass-forming region and physical properties of the glasses in the TeO₂-MoO₃-Bi₂O₃ system. *Journal of Non-Crystalline Solids*, 452, 130-135. Doi: 10.1016/j.jnoncrsol.2016.08.027
- Brundle C. R., Chuang T. J., Wandelt K. (1977): Core and valence level photoemission studies of iron oxide surfaces and the oxidation of iron. *Surface Science*, 68, 459-468. Doi:10.1016/0039-6028(77)90239-4
- Mekki A., Salim M. (1999): XPS study of transition metal doped silicate glasses. *Journal of Electron Spectroscopy and Related Phenomena*, 101, 227-232. Doi: 10.1016/S0368-2048(98)00450-2
- Yamashita T., Hayes P. (2008): Analysis of XPS spectra of Fe²⁺ and Fe³⁺ ions in oxide materials. *Applied Surface Science*, 254(8), 2441-2449. Doi:10.1016/j.apsusc.2007.09.063
- Chen M., Liu J., Wu Z. (2022): Effect of Fe₂O₃ Concentration on the Properties of Basalt Glasses. *Journal of Natural Fibers*, 19(2), 575-585. Doi: 10.1080/15440478.2020.1758277
- Clayden N. J., Esposito S., Aronne A., Pernice P. (1999): Solid state ²⁷Al NMR and FTIR study of lanthanum aluminosilicate glasses. *Journal of Non-Crystalline Solids*, 258(1-3), 11-19. Doi: 10.1016/S0022-3093(99)00555-4
- Liu J., Jiang M., Wang Y., Wu G., Wu Z. (2013): Tensile behaviors of ECR-glass and high strength glass fibers after NaOH treatment. *Ceramics International*, 39(8), 9173-9178. Doi: 10.1016/j.ceramint.2013.05.018
- Lubas M., Sitarz M., Fojud Z., Jurga S. (2005): Structure of multicomponent SiO₂-Al₂O₃-Fe₂O₃-CaO-MgO glasses for the preparation of fibrous insulating materials. *Journal of Molecular Structure*, 744, 615-619. Doi:10.1016/j.molstruc.2004.12.011
- Dantas N. O., Ayta W. E., Silva A. C., Cano N. F., Silva S. W., Morais P. C. (2011): Effect of Fe₂O₃ concentration on the structure of the SiO₂-Na₂O-Al₂O₃-B₂O₃ glass system. *Spectrochimica Acta Part A: Molecular and Biomolecular Spectroscopy*, 81(1), 140-143. Doi: 10.1016/j.saa.2011.05.074
- Monisha M., Murari M. S., Sayyed M. I., Al-Ghamdi H., Almuqrin A. H., Lakshminarayana G., Kamath S. D. (2021): Thermal, structural and optical behaviour of Eu³⁺ ions in Zinc Alumino Boro-Silicate glasses for bright red emissions. *Materials Chemistry and Physics*, 270, 124787. Doi: 10.1016/j.matchemphys.2021.124787
- Wang Q., Zhang Q., Luo L., Yan T., Liu J., Ding L., Jiang W. (2021): Effects of high-temperature treatment and iron reduction index on tensile strength of basalt continuous fiber. *Journal of Non-Crystalline Solids*, 564, 120836. Doi: 10.1016/j.jnoncrsol.2021.120836
- Smedskjaer M. M., Solvang M., Yue Y. (2010): Crystallisation behaviour and high-temperature stability of stone wool

- fibres. *Journal of the European Ceramic Society*, 30(6), 1287-1295. Doi: 10.1016/j.jeurceramsoc.2009.12.009
28. Gutnikov S. I., Manylov M. S., Lipatov Y. V., Lazoryak B. I., Pokholok K. V. (2013): Effect of the reduction treatment on the basalt continuous fiber crystallization properties. *Journal of Non-Crystalline Solids*, 368, 45-50. Doi: 10.1016/j.jnoncrysol.2013.03.007
29. Das C. R. (1981): Chemical durability of sodium silicate glasses containing Al_2O_3 and ZrO_2 . *Journal of the American Ceramic Society*, 64(4), 188-193. Doi: 10.1111/j.1151-2916.1981.tb10266.x
30. Scheffler C., Förster T., Mäder E., Heinrich G., Hempel S., Mechtcherine V. (2009): Aging of alkali-resistant glass and basalt fibers in alkaline solutions: Evaluation of the failure stress by Weibull distribution function. *Journal of Non-Crystalline Solids*, 355(52-54), 2588-2595. Doi: 10.1016/j.jnoncrysol.2009.09.018
31. Dhir R. K., Dyer T. D., Tang M. C. (2009): Alkali-silica reaction in concrete containing glass. *Materials and Structures*, 42, 1451-1462. Doi: 10.1617/s11527-008-9465-8
32. Liu Z. B., Zong Y. B., Ma H. Y., Dai W. B., Li S. H. (2014): Effect of $(CaO+MgO)/SiO_2$ ratio on crystallisation and properties of slag glass-ceramics. *Advances in Applied Ceramics*, 113(7), 411-418. Doi:10.1179/1743676114y.0000000187
33. Mechtcherine V., Lieboldt M. (2011): Permeation of water and gases through cracked textile reinforced concrete. *Cement and Concrete Composites*, 33(7), 725-734. Doi: 10.1016/j.cemconcomp.2011.04.001
34. Lipatov Y. V., Gutnikov S. I., Manylov M. S., Zhukovskaya E. S., Lazoryak B. I. (2015): High alkali-resistant basalt fiber for reinforcing concrete. *Materials & Design*, 73, 60-66. Doi:10.1016/j.matdes.2015.02.022
35. Li D., Ding Y., Wang Q., Zhang Y., Azevedo C., Zhang Y. (2019): Hybrid effect of fibre mesh and short fibres on the biaxial bending behaviour of TRC. *Magazine of Concrete Research*, 71(16), 869-880. Doi: 10.1680/JMACR.17.00284
36. Liu H. P., Huang X. F., Ma L. P., Chen D. L., Shang Z. B., Jiang M. (2017): Effect of Fe_2O_3 on the crystallization behavior of glass-ceramics produced from naturally cooled yellow phosphorus furnace slag. *International Journal of Minerals, Metallurgy, and Materials*, 24, 316-323. Doi: 10.1007/s12613-017-1410-9
37. Wang Q., Ding Y., Rand N. (2021): Investigation on the alkali resistance of basalt fiber and its textile in different alkaline environments. *Construction and Building Materials*, 272, 121670. Doi: 10.1016/j.conbuildmat.2020.121670
38. Manylov M. S., Gutnikov S. I., Lipatov Y. V., Malakho A. P., Lazoryak B. I. (2015): Effect of deferrization on continuous basalt fiber properties. *Mendeleev Communications*, 5(25), 386-388. Doi: 10.1016/j.mencom.2015.09.025
-